

Deep turbulence effects compensation experiments with a cascaded adaptive optics system using a 3.63 m telescope

Mikhail Vorontsov,^{1,2,*} Jim Riker,³ Gary Carhart,¹ V. S. Rao Gudimetla,⁴
Leonid Beresnev,¹ Thomas Weyrauch,² and Lewis C. Roberts, Jr.⁵

¹Intelligent Optics Laboratory, Computational and Information Sciences Directorate,
U.S. Army Research Laboratory, Adelphi, Maryland 20783, USA

²Intelligent Optics Laboratory, Institute for Systems Research,
University of Maryland, College Park, Maryland 20742, USA

³U.S. Air Force Research Laboratory, 3550 Aberdeen Avenue SE, Kirtland AFB, New Mexico 87117, USA

⁴U.S. Air Force Research Laboratory, Detachment 15, 535 Lipoa Parkway, Kehie, Hawaii 96753, USA

⁵The Boeing Company, 535 Lipoa Parkway, Suite 200, Kihei, Hawaii 96753, USA

*Corresponding author: mvorontsov@arl.army.mil

Received 17 June 2008; revised 30 September 2008; accepted 1 October 2008;
posted 8 October 2008 (Doc. ID 97497); published 7 November 2008

Compensation of extended (deep) turbulence effects is one of the most challenging problems in adaptive optics (AO). In the AO approach described, the deep turbulence wave propagation regime was achieved by imaging stars at low elevation angles when image quality improvement with conventional AO was poor. These experiments were conducted at the U.S. Air Force Maui Optical and Supercomputing Site (AMOS) by using the 3.63 m telescope located on Haleakala, Maui. To enhance compensation performance we used a cascaded AO system composed of a conventional AO system based on a Shack–Hartmann wavefront sensor and a deformable mirror with 941 actuators, and an AO system based on stochastic parallel gradient descent optimization with four deformable mirrors (75 control channels). This first-time field demonstration of a cascaded AO system achieved considerably improved performance of wavefront phase aberration compensation. Image quality was improved in a repeatable way in the presence of stressing atmospheric conditions obtained by using stars at elevation angles as low as 15°. © 2009 Optical Society of America

OCIS codes: 010.1080, 010.1290, 140.3290, 140.3298, 140.3510.

1. Introduction

In imaging of astronomical or space objects located at high elevation angles, atmospheric turbulence can be considered to be a thin pupil-plane distorting layer that affects only the received wave phase—the so-called low-scintillation optical wave propagation regime [1]. The phase aberrations introduced by this pupil-plane turbulence layer can be mitigated by

using conventional (astronomical) adaptive optics (AO) compensation techniques based on wavefront sensor measurements that are used for computation of the control signals applied to wavefront corrector (deformable or segmented mirror) actuators [2,3].

For propagation through volume (deep) turbulence typical for observation of low-elevation-angle space objects and near-ground atmospheric optics applications, such as laser beam projection, free-space laser communication, imaging, and tracking, this conventional AO (C_AO) approach can be inefficient [4]. Several well-known factors contribute to the

degradation of AO system performance under deep turbulence conditions.

First, wave propagation in volume turbulence commonly results in strong intensity scintillations at the telescope aperture, leading to an increase of the noise level in wavefront sensor measurements in regions of low intensity. In turn this results in the appearance of errors in control signal computation [5,6]. Second, these intensity scintillations are commonly accompanied by discontinuities in the received wavefront phase known as wavefront dislocations (branch points) [7–9]. These phase singularities are difficult to approximate and hence compensate by using conventional wavefront correctors—continuously deformable or segmented adaptive mirrors. Finally, turbulence-induced optical inhomogeneities that are distributed along the propagation path result in the dependence of phase aberrations on the input wave angle of arrival—an effect known as anisoplanatism—and the narrowing of the AO system field of view associated with this effect [10,11]. These factors make compensation of deep turbulence effects one of the most challenging problems in AO [4].

In the AO experiments described in this paper, the deep turbulence wave propagation regime was achieved by imaging stars at low elevation angles below 45°–50° when image quality improvement with the C_AO system was poor. To enhance the compensation performance we combined in a cascade both a C_AO system based on a Shack–Hartmann wavefront sensor, and an AO technique that does not require measurements of wavefront phase characteristics (slopes, local curvatures, etc.), known as the stochastic parallel gradient descent optimization technique (SPGD_AO) [12,13]. These experiments were performed by using the 3.63 m telescope located on Haleakala on the island of Maui [14].

The SPGD_AO technique was proved to be more resilient to intensity scintillations than the C_AO technique but requires significantly higher operational bandwidth owing to the iterative nature of the control algorithm [4,15,16].

Note that in all experiments performed by using stars at high elevation angles (commonly exceeding 45°–50°, dependent on atmospheric conditions), the C_AO system provided near-diffraction-limited image quality, which could not be achieved with the SPGD_AO system alone. However, in the experiments with the low-elevation stars (elevation angles between 15° and 45°) the SPGD_AO system was able to demonstrate a significant improvement in image quality. The results presented provide a direct comparison of these two wavefront control approaches under various atmospheric conditions with the main emphasis on compensation of volume turbulence effects.

The most general conclusion derived from these experiments is that under the deep turbulence conditions there is a significant benefit to using both C_AO and SPGD_AO techniques operating simultaneously in a cascade. From this viewpoint the experi-

mental results presented provide the first arguments for the future development of a new generation of cascaded AO systems.

2. Cascaded Adaptive Optics System: Experimental Setup

A. Experimental Setup and Major Subsystems

The experiments were performed using the U.S. Air Force Maui Optical and Supercomputing Site (AMOS) facilities at Mount Haleakala. A simplified (notional) block diagram of the experimental setup is shown in Fig. 1. The system is composed of the 3.63 m telescope equipped with the C_AO system described in [17], also referred to as the Advanced Electro-Optical System (AEOS), and the adaptive system based on SPGD_AO located on an optical table in one of the AMOS Coude rooms. For convenience of graphical representation in Fig. 1, wavefront correctors in both C_AO and SPGD_AO systems are shown as transmissive optical elements (DM_{CAO} and DM_{SPGD}), while in the actual system only reflective elements were used.

The C_AO system is composed of the deformable mirror DM_{CAO} with 941 actuators, the Shack–Hartmann wavefront sensor (WFS) and its control electronics (C_AO controller) [17]. The conventional AO system operated in the visible wavelength band, while compensation of the residual phase aberrations by the SPGD_AO system was performed in the near-infrared (NIR) band (0.9–1.7 μm).

The phase of the input optical wave was corrected by the C_AO system. The corrected output wave was divided by the dichroic beam splitter (DBS) in Fig. 1 into visible and NIR components. The visible light

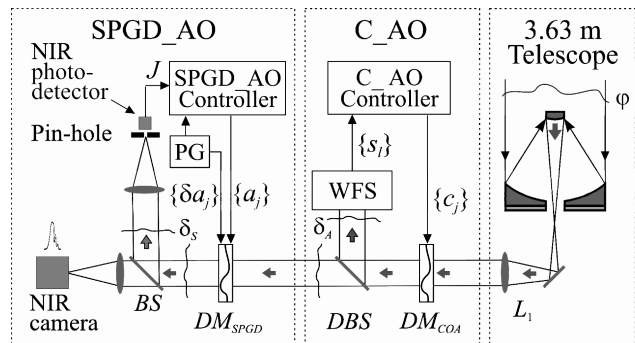


Fig. 1. Notional schematic of the cascaded AO imaging system composed of the conventional adaptive system (C_AO) and the SPGD system (SPGD_AO). The residual wavefront phase δ_A in the C_AO system is analyzed by the Shack–Hartmann wavefront sensor (WFS), and the sensor's output signals $\{S_i\}$ are sent to the controller (C_AO controller) that provides control voltages $\{c_j\}$ applied to the actuators of the deformable mirror DM_{COA} . In the SPGD_AO system the corrected optical wave with residual phase aberration δ_S is focused into a pinhole. The SPGD controller (SPGD_AO controller) uses the measurement of the signal J received through the pinhole as an input to compute control voltages $\{a_j\}$ applied to the deformable mirrors shown as a single transmissive optical element DM_{SPGD} . The perturbation generator (PG) supplies small amplitude control voltages $\{\delta a_j\}$ to both deformable mirrors DM_{SPGD} and the SPGD controller.

component reflected by the beam splitter entered the wavefront sensor of the C_AO system used to control the deformable mirror DM_{CAO} . The NIR optical wave component entered the Coude port and was used as the SPGD_AO system input beam as shown in Fig. 1.

This input beam passed through the set of four controllable mirrors of the SPGD_AO system indicated in Fig. 1 as a single phase correcting element (DM_{SPGD}). The corrected wave then entered a beam splitter (BS). The portion of the light transmitted by the beam splitter ($\sim 50\%$) was used to record short-exposure (integration time 4 ms) corrected images of the star by using a NIR camera. The light reflected from the beam splitter entered the metric sensor.

The metric sensor was composed of a lens with a small pinhole located in its focal plane. The output voltage of the photodetector, J , was used as a measure of the SPGD_AO system performance (performance metric). The signal J was sent to the SPGD_AO controller and was used to compute the control voltages $\{a_j\}, j = 1, \dots, N$ applied to all wavefront corrector electrodes (total $N = 75$ control channels).

B. SPGD Adaptive Optics System

The SPGD_AO system schematic is shown in Fig. 2. The input optical beam of diameter 100 mm was reflected from two flat mirrors (not shown) used for alignment of the SPGD_AO system optical axis and then from the pocket deformable mirror (PM) located approximately in an image plane of the telescope pupil. An optical reducer composed of the off-axis parabolic mirror pair (OAP_1 and OAP_2) reimaged the plane of the pocket mirror onto the first deformable mirror (DM_1) with fourfold demagnification. The optical beam, reduced to diameter 25 mm, propagated to the second deformable mirror (DM_2)

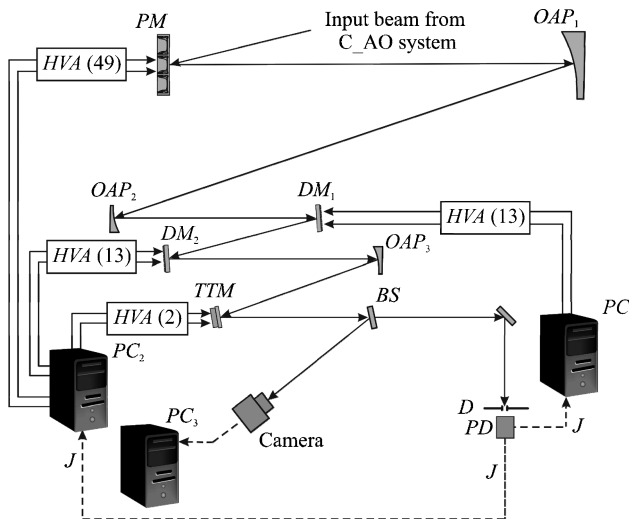


Fig. 2. Schematic of the SPGD adaptive system. The system is composed of the pocket mirror PM, two deformable mirrors DM_1 and DM_2 , tip-tilt (beam steering) mirror TTM, off-axis parabolic mirrors OAP_1 – OAP_3 , beam splitter BS, pinhole D, photodetector PD, and a NIR CCD camera. The SPGD control system includes personal computers PC_1 – PC_3 and high-voltage amplifiers HVA (number of control channels is indicated in parentheses).

and after reflection from its surface entered the off-axis parabolic mirror (OAP_3) with a focal distance equal to 350 mm.

The reflected converging optical wave was directed onto a flat mirror mounted on a tip-tilt platform (TTM) located 33 mm from the OAP_3 mirror. The tip-tilt mirror was used for automated steering of the focal spot for alignment purposes as well as for compensation of the turbulence-induced tip-tilt wavefront phase aberration components. The beam reflected from the tip-tilt mirror was equally divided by the beam splitter (BS) to form an image of the observed star at both the photoarray of the NIR camera and the pinhole as shown in Fig. 2. The star images were recorded with a frame rate of 220 frames/s and spatial resolution of 256×256 . The camera pixel size was $25 \mu\text{m}$, and the fill factor was 100%. The diffraction-limited focal spot size (Airy spot diameter) was $90 \mu\text{m}$.

The photodetector was located approximately 3 mm behind the pinhole. In the experiments we used pinholes of three different diameters: 100, 150, and $200 \mu\text{m}$.

A single-pixel photodetector with an active area of $1 \text{ mm} \times 1 \text{ mm}$ was used to measure the optical power P that passed through the pinhole. The output voltage J of the photodetector used is proportional to the logarithm of received power P , so that $J = c \log(\alpha P + P_0)$, where c , α , and P_0 are parameters of the photodetector (bias voltage and signal amplification coefficients).

C. Wavefront Correctors

In the SPGD_AO system, the following three wavefront correctors were used: a single pocket deformable mirror (PM) of diameter 100 mm and two deformable mirrors (DM_1 and DM_2) of diameter 25 mm. The operational bandwidth was 15 KHz for the pocket mirror and 12 KHz for both deformable mirrors. All three wavefront correctors are based on semipassive piezo-ceramic bimorph elements and were designed and manufactured at the Army Research Laboratory Intelligent Optics Laboratory [18,19].

The pocket deformable mirror (PM) in Fig. 3 was used for compensation of low-order aberrations inside seven densely packed hexagonal regions (pockets) machined into a 25 mm thick glass blank [18]. A photograph of the back (machined) side of the pocket mirror is shown in Fig. 3(a). The front surface of the mirror had a reflective layer of deposited silver. Deformation of the deformable mirror surface inside each pocket resulted from voltages applied to seven electrodes patterned on one side of a thin piezo-ceramic disk attached to the back side of the mirror. The pattern of the pocket mirror electrodes is shown in Fig. 3(b). An example of the pocket mirror surface deformation in response to equal control voltages (70 V) applied to a single electrode in each pocket (marked by stars in Fig. 3(b)) is illustrated in Fig. 3(c) as the mirror surface interference pattern and in

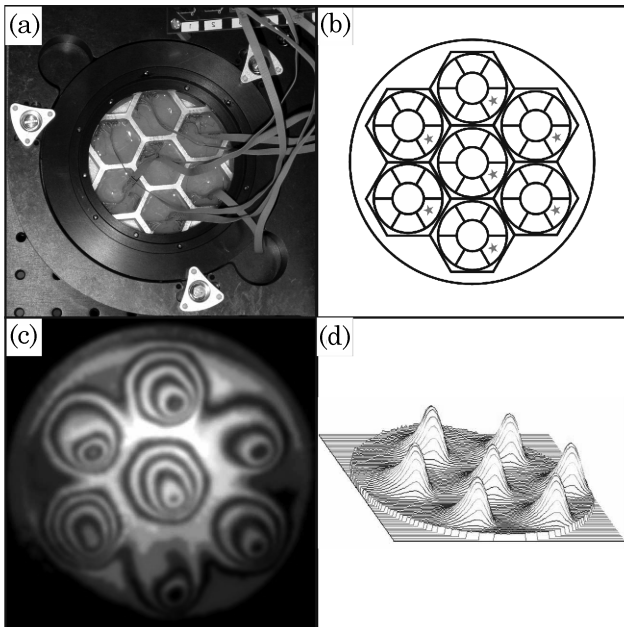


Fig. 3. Pocket deformable mirror (PM): (a) photograph of the back side of PM with seven machined pockets, (b) geometry of seven electrodes inside each pocket, (c) an interference pattern, (d) the 3D phase pattern reconstructed from the interferogram in (c). In (c) and (d) static control signals with the amplitude 90 V were applied to the electrodes indicated by the stars in (b), and zero control signals to the remaining electrodes.

Fig. 3(d) as a 3D phase function. The pocket mirror maximum stroke was approximately equal to $8\ \mu\text{m}$ when 90 V was applied to all the electrodes of a pocket and approximately $5\ \mu\text{m}$ when an equal control voltage was applied to only a single electrode.

Low-order phase aberrations were compensated by using two identical deformable mirrors (DM_1 and DM_2), also based on semipassive bimorph piezoceramic elements [2]. One of the mirrors is shown in Fig. 4(a). The mirrors were rotated with respect to each other by 30° about the optical axis to minimize overlapping of their response functions. The geometry of 13 electrodes patterned on the back of the piezo-ceramic disk attached to the glass plate and the example of the mirror surface deformation are shown in Figs. 4(b)–4(d). The stroke of surface deformation for the deformable mirrors was nearly identical to the pocket mirror.

D. Compensation of Static and Atmospheric-Averaged Aberrations

The deformable mirror DM_1 was used for compensation of atmospheric turbulence-induced large-scale aberrations. The second deformable mirror (DM_2) was included for compensation of static phase aberrations originating from imperfect alignment of optical elements in the entire optical train. Such compensation of the static phase aberrations is needed to preserve the full dynamical range of the first deformable mirror for compensation of solely atmospheric turbulence-induced phase distortions. The static phase aberration in the SPGD_AO system

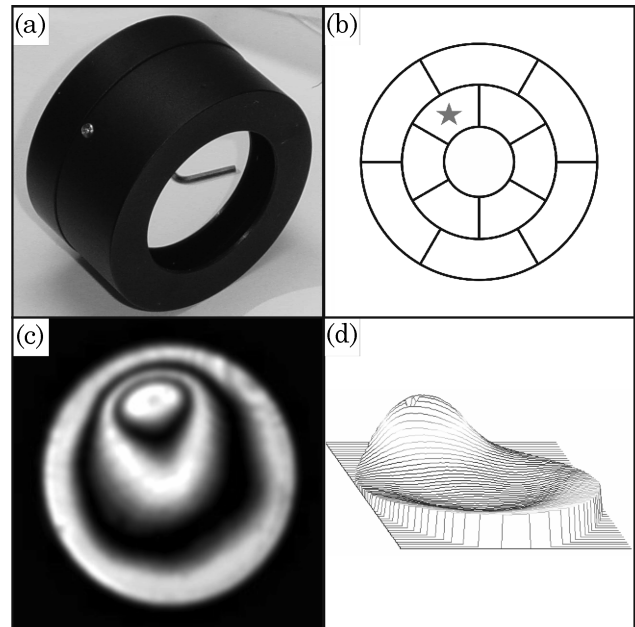


Fig. 4. Deformable mirror (DM): (a) photograph of the front side of DM with aperture 25 mm, (b) geometry of 13 electrodes, (c) an interference pattern, (d) the 3D phase pattern reconstructed from the interferogram in (c). The patterns in (c) and (d) illustrate the phase aberration introduced by the deformable mirror corresponding to a static control signal with an amplitude of 90 V applied to the electrode indicated by the star in (b), and zero control signals to the remaining electrodes.

(composed mostly of defocus and astigmatism) was of the order of $0.6\ \mu\text{m}$ (peak-to-valley value). The static aberration was precompensated by using an optical beam from the Zygo interferometer as an input for the SPGD_AO system. During static aberration compensation we set to zero the control voltages on the first deformable mirror (DM_1) while both DM_2 and the pocket mirrors were included in the SPGD adaptation process leading to the metric J maximization. The voltages obtained at the end of the optimization process were used as a reference.

In the course of the experiments we observed the presence of an additional slowly varying (quasi-static) phase aberration (in the range near $10\ \mu\text{m}$) related to the rotation of the telescope during star tracking and related to wind pressure on the dome. To compensate for this quasi-static aberration we used an additional SPGD control loop, referred to here as the atmospheric-averaged SPGD control. The atmospheric-averaged control was based on measurements and averaging of a large number (~ 100) of metric J values performed with the time delay $\Delta t = 0.1\ \text{s}$, which significantly exceeds the characteristic time τ_{at} of atmospheric turbulence change. The atmospheric-averaging control was used to find the shape of the deformable mirror DM_2 prior to turning on the main (fast) SPGD control by maximizing the averaged value of the performance metric $\langle J \rangle$. After metric $\langle J \rangle$ was optimized, the corresponding control voltages on the deformable mirror DM_2 were fixed and used as initial conditions

for the fast SPGD control loop. This technique allowed us accurately to estimate the image quality improvement associated solely with atmospheric turbulence compensation.

The second function of the deformable mirror DM₂ was to add more capabilities in the spatial resolution and dynamical range for atmospheric turbulence compensation. In this regime both DM₁ and DM₂ were used for atmospheric aberration compensation with maximum possible speed. Both mirrors were driven by two independent and asynchronously operated SPGD controllers using the single metric J . The asynchronous SPGD control approach is described in [20].

E. Feedback Control: System and Algorithms

The control system consisted of four SPGD controllers driving one pocket mirror, two deformable mirrors, and one tip-tilt mirror (see Fig. 2). The control system was implemented by using 2.2 GHz personal computers (PC₁ and PC₂), each equipped with analog input and output cards. One computer (PC₁) was used to control only the deformable mirror DM₁ (13 control channels), while the second computer (PC₂) controlled both the pocket mirror (49 control channels), the second deformable mirror DM₂ (13 control channels) and the tip-tilt mirror (2 channels). These three mirrors operated as part of a single 64-channel SPGD_AO control system (or a 13-, 49-, or 2-channel SPGD_AO system when only one of these correctors was used). The operational speed was dependent on the control system configuration. A set of high-voltage amplifiers was used to amplify control signals to the range $[-100v, 100v]$. The SPGD control systems based on PC₁ and PC₂ controllers operated asynchronously, using the same metric signal.

In both SPGD_AO systems the control voltage update was performed by using the following iterative update rule [4,15]:

$$a_j^{(n+1)} = a_j^{(n)} + \gamma^{(n)} \delta \alpha_j^{(n)} \delta J^{(n)} \quad (J = 1, \dots, N),$$

$$n = 1, \dots, \quad (1)$$

where N is the number of control channels, $\delta \alpha_j^{(n)} = \kappa^{(n)} \delta P_j^{(n)}$ is a small amplitude voltage perturbation applied to the deformable mirror (DM₁, DM₂, PM, or TTM) j th actuator at the n th iteration, $\kappa^{(n)}$ is the perturbation amplitude, $\gamma^{(n)}$ is the gain coefficient, and $\delta J^{(n)}$ is the metric perturbation. Here $\{\delta p_j^{(n)}\}$ are a precalculated set of random numbers with zero mean and Bernoulli (coin-type) probability distribution. A second option for the perturbations was the use of a set of random numbers with zero mean and probability distribution corresponding to an approximation of Kolmogorov phase screen realizations using Zernike coefficients [20]. For either SPGD_AO system, the control voltage perturbations were simultaneously applied to all wavefront corrector actuators. The voltage perturbations are used to calculate the metric perturbation $\delta J^{(n)}$.

In the version of the SPGD algorithm implemented, the gain coefficient $\gamma^{(n)}$ and the perturbation amplitude $\kappa^{(n)}$ were functions of the current metric value $J^{(n)}$ [14]:

$$\gamma^{(n)} = \gamma_0 \left(\frac{J_{\text{opt}}}{J_{\text{opt}} + J^{(n)}} \right), \quad \kappa^{(n)} = \kappa_0 \left(\frac{J_{\text{opt}}}{J_{\text{opt}} + J^{(n)}} \right)^q, \quad (2)$$

where J_{opt} is a predetermined (expected) maximum metric value, γ_0 and κ_0 are gain and perturbation amplitude coefficients, and p and q are numbers controlling the rate of the metric change. Functional dependences (2) scale the gain and perturbation amplitude so that the SPGD controller uses larger amplitude perturbations and gain coefficient when the metric is smaller than J_{opt} and smaller ones when it is near its expected optimum value J_{opt} . The four parameters p , q , γ_0 , and κ_0 in control rule (2) were selected separately for each wavefront corrector used.

The maximum iteration rate for the SPGD controller PC₁ operating with the single 13-electrode deformable mirror (DM₁) was approximately 9000 iterations per second, while the iteration rate of the second SPGD control system (controller PC₂) was 6000 iterations per second.

3. Atmospheric Compensation with Cascaded AO System

A. Operational Regimes

The experiments with the cascaded AO system were performed from 17 May until 30 May 2007 between 8:30 p.m. and midnight. As light sources for imaging we used several bright stars in the near infrared bandwidth: the first magnitude stars Antares (HR 6134) and Arcturus (HR 5340) observed, respectively, at elevation angles between 8° and 30° and between 50° and 80° and the third magnitude star Delta Ophiuchi (HR 6056) near 45° elevation.

Viewing conditions were changing from night to night and during the observation time. The compensation performance was very much dependent on these conditions as well as on the elevation of the imaging star. For this reason the parameters of the SPGD_AO were optimized several times during the night to achieve the best possible image quality improvement. Clouds and strong wind during several observation nights resulted in poor performance of both AO systems. The data presented were collected under good observation conditions (clear nights with relatively low wind speed).

It was possible to turn on and off both the C_AO and the SPGD_AO systems during experiments and thus proceed with measurements corresponding to the following operational regimes:

1. **OFF/OFF** regime. Both C_AO and the SPGD_AO controllers are off.

2. **ON/OFF** regime. The C_AO system is on and the SPGD_AO controllers are off.

3. **OFF/PC₂** regime. The C_AO is off, and the SPGD_AO subsystem PC₂ that includes the deformable mirror DM₂ and the pocket mirror PM is on.

4. **ON/ON** regime. Both the C_AO and all the SPGD_AO controllers are on.

Note that prior to the SPGD system operation (**OFF/PC₂** and **ON/ON** regimes) we used the atmospheric-average SPGD optimization of the metric $\langle J \rangle$ as described in Section 2.D. This allowed us to find control voltages $\{a_j^{\text{aver}}\}$ ($j = 1, \dots, 13$) for the deformable mirror DM₁ corresponding to precompensation of static phase aberrations. These voltages were fixed during the SPGD system operation.

B. Adaptation Trials and Data Analysis

Adaptive system performance estimation and control parameter optimization were based on the following procedure referred to here as the *adaptation trial*. The adaptation trial was composed of a large number M of SPGD iterations ($M = 4 \times 10^4 - 8 \times 10^4$) that lasted about 4 or 8 s and included the following sequential phases ($M/4$ iterations each):

a. **SPGD_OFF** phase. During this phase the SPGD controllers were off and the voltages on both the pocket mirror and both deformable mirrors were fixed. These control voltages are referred to as initial conditions.

b. **DM_ONLY** phase. In this phase the control voltages on the pocket mirror were fixed and the SPGD controller updated only 13 control voltages of the deformable mirror DM₂.

c. **PM&DM**. During this phase the SPGD controller updated voltages on both the DM₂ and PM wavefront correctors.

d. **PM_ONLY** phase. In this phase the SPGD controller (PC₂) updated only the control voltages applied to the pocket mirror and the voltages on both deformable mirrors were fixed.

During the adaptation trial the metric values $J(m)$ measured at each SPGD iteration ($m = 1, \dots, M$), were recorded. Because the actual adaptation rate was also recorded, the temporal behavior of the optimized metric $J(t)$ can be easily obtained from the measured dependence $J(m)$. A typical time dependence of metric $J(t)$ during a single adaptation trial is shown in Fig. 5(a). Continuous changes in the atmospheric turbulence conditions resulted in strong variations in the adaptation trials.

To decrease the dependence of the compensation performance on varying atmospheric conditions, a large number (typically ~30–50) of sequential adaptation trials were recorded and averaged.

An example of the averaged adaptation curve $\langle J(t) \rangle$ obtained in the cascaded AO system is shown in Fig. 5(b). The averaged curve shows noticeable improvement achieved by using the additional SPGD-

based AO system. Note that the metric J is logarithmically dependent on the received power inside the pinhole.

As seen in Fig. 5, the best performance was achieved when the SPGD controller was used to drive solely the deformable mirror DM₂ with static voltages applied to the pocket mirror (**DM_ONLY** phase). This compensation efficiency decrease with the closing of an additional feedback loop with the pocket mirror was quite typical and can be partially explained by a 15%–20% decrease in the adaptation rate observed when the additional 49 channels of the pocket mirror were included in the SPGD feedback loop, since a single computer (PC₂ in Fig. 2) was used to drive both the deformable and pocket mirrors.

This problem can be resolved by having independent asynchronously operating SPGD processors for the deformable and pocket mirrors. Unfortunately, we did not have the opportunity to rearrange control loops directly during the experimental campaign. Nevertheless, in some cases (low-wind and weak-turbulence conditions) we did observe noticeable improvement when the pocket mirror was

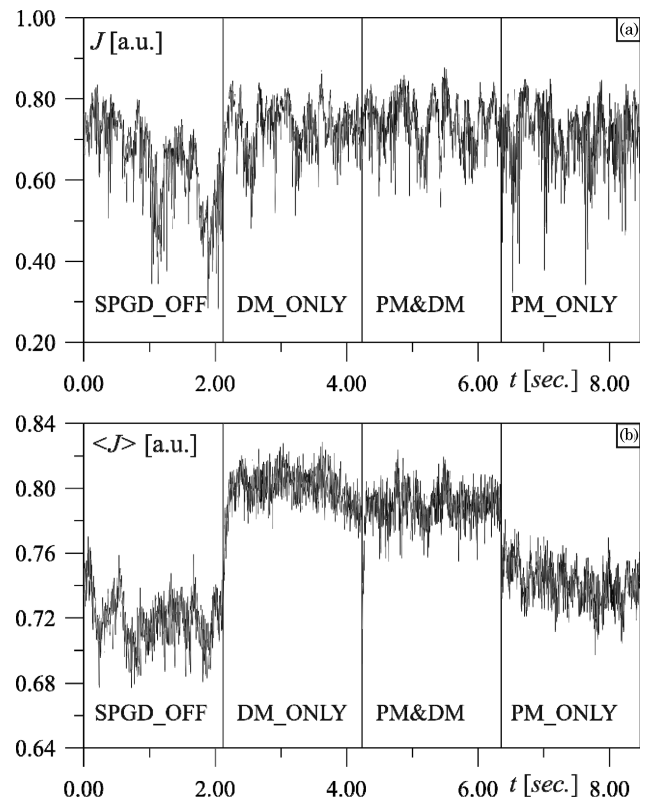


Fig. 5. Characteristic examples of metric J time dependence corresponding to single (a) and averaged (b) adaptation trials composed of the following four adaptation phases: the SPGD AO system turned off (SPGD_OFF), the SPGD system operating with only deformable mirror DM₂ active (DM_ONLY), with the corresponding system operating with both the PM and DM₂ mirrors active (PM&DM), and with only the PM (PM_ONLY) active. The pinhole size is equal to 150 μm . The light source was Antares at elevation angle 16°. The C_AO system (AEOS) was on for all cases. In all four adaptation phases the control voltages applied to the deformable mirror DM₁ were fixed.

included in the SPGD feedback loop together with the deformable mirror.

During the adaptation trials we computed metric histograms $h(J)$ corresponding to each of the four operational phases. Here h is the number of events that occurred during the corresponding adaptation phase for which the measured metric value belonged to the interval $[J, J + \Delta J]$. The metric interval ΔJ (metric bin) corresponded to (1/512)th of the entire dynamical range in metric signal measurements. Averaged over the large number of adaptation trials, these histograms characterize the probability distribution of metric values. The averaged histograms $p_J(J) \equiv \langle h(J) \rangle$ were typically computed using about 10^6 metric measurements.

For comparison of compensation efficiency using either the cascaded or one of the two AO systems (conventional or SPGD) alone under nearly identical atmospheric conditions, the metric histograms were recorded for the four subsequent feedback ON and OFF regimes for both conventional and SPGD systems as described in Section 3.A. Still, because the duration of data collection lasted about 3–6 min for each histogram—long enough on the time scale of atmospheric conditions change—an accurate efficiency analysis can be made only by repeating the same set of experiments many times. Unfortunately several other factors, such as changing weather conditions and elevation of the star, further complicate this comparison. For this reason the data obtained can only provide a ballpark comparison of the compensation efficiency between cascaded and one of the two (conventional and SPGD) AO systems.

C. Analysis of Compensation Efficiency Based on Metric Data

Examples of the metric histograms corresponding to the four adaptation trial phases with the inactive C_AO system are presented in Figs. 6(a) and 6(b). To mitigate the effect of the quasi-static aberrations emerging during data collection, we used the following procedure to reset the control voltages for both the pocket and deformable mirror DM₂ at the beginning of each of the four phases of each adaptation trial. At the end of each trial we calculated averaged control voltages for each phase separately and used these averaged voltages at the beginning of the corresponding phases for the next adaptation trial.

During the entire time of data collection, the control voltages applied to the deformable mirror DM₁ were fixed. These voltages (initial conditions) were obtained prior to data collection by optimizing either metric J , using a reference source (light beam from a Zygo interferometer) in Fig. 6(a) or the atmospheric average metric $\langle J \rangle$ using the star as the light source in Fig 6(b).

The histograms with the preset [Fig. 6(a)] and the atmospheric-averaged [Fig. 6(b)] initial conditions show clearly that the initial conditions play an important role in the true estimation of the atmospheric compensation efficiency. Indeed, in Fig. 6 compare

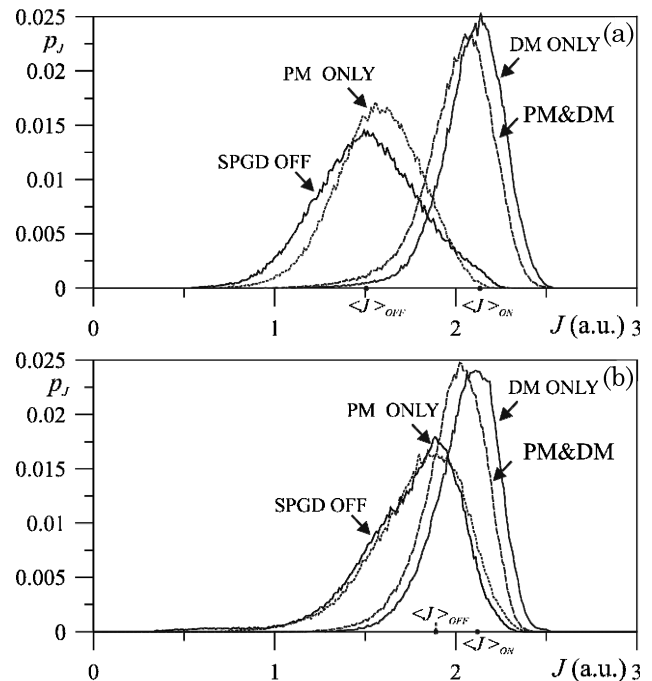


Fig. 6. Probability distributions p_J versus metric J in arbitrary units (a.u.) obtained by averaging 50 adaptation trials for different adaptation phases: (a) without and (b) with quasi-static (atmospheric averaged) phase aberration compensation. The corresponding data were recorded with the C_AO system off, using Antares as a light source at an elevation angle between 16° and 18° . The SPGD adaptation rate was about 6000 iterations per second. The pinhole size for metric measurements was $200\ \mu\text{m}$. Note that compensation of quasi-static aberration in (b) resulted in a noticeable shift toward bigger metric values (to the right) in the probability distribution curve, corresponding to the SPGD OFF regime.

both the averaged metric values $\langle J \rangle_{\text{OFF}}$ (SPGD OFF phase) and $\langle J \rangle_{\text{ON}}$ (PM&DM phase) that correspond to the histogram (probability density) curve maximum and the histogram curve width that characterizes the standard deviation of metric fluctuations. In both cases in Fig. 6 adaptive compensation results in the increase of the corresponding averaged metric value $\langle J \rangle_{\text{ON}}$ and the decrease of the metric fluctuations. Nevertheless, when the quasi-static aberrations are precompensated by using the atmospheric-averaged initial conditions, the obtained averaged metric values $\langle J \rangle_{\text{OFF}}$ in Fig. 6(b) are significantly bigger than the corresponding metric value in Fig. 6(a) obtained with the preset initial conditions. Correspondingly the true gain in the metric value increase related solely to the atmospheric turbulence effects compensation, as measured by the ratio $g = (\langle J \rangle_{\text{ON}} - \langle J \rangle_{\text{OFF}}) / \langle J \rangle_{\text{ON}}$, is evidently smaller when quasi-static aberrations are removed by using atmospheric-average initial conditions in Fig. 6(b). Note also that the histograms in Fig. 6 show that the use of both the deformable and pocket mirror resulted in a decrease of the compensation performance that had been achieved with SPGD control of the deformable mirror only. This

result can be explained by taking into account two factors: the decrease of the iteration rate when the pocket mirror was included in the SPGD controller operation, as discussed in Section 2.E, and competition in compensating large-scale aberrations (wavefront tilts, defocus, astigmatism, etc.) between control channels driving the deformable and pocket mirrors. These aberrations can be better (more accurately) mitigated by the deformable mirror than by the pocket mirror. Correspondingly, operation of both mirrors is more likely to lead to the appearance of metric local extrema and performance degradation. This unwanted effect can potentially be mitigated by a faster operating control system for the deformable mirror so that low-order aberrations are primarily compensated by the deformable mirror before the pocket mirror can respond. As already mentioned, we also observed adaptation trials for which operation with both the deformable and the pocket mirrors resulted in better compensation as illustrated in Fig. 7(a). The general observation is that the compensation efficiency when all three mirrors are used simultaneously was quite sensitive to the chosen

parameters of the SPGD controllers and the turbulence strength.

A characteristic example of the SPGD compensation performance using the two SPGD control systems with three wavefront correctors (DM₁, DM₂, and pocket mirror) is shown in Fig. 7(b). Both SPGD control systems PC₁ and PC₂ in Fig. 2 were operating asynchronously with the iteration rates of 9000 and 6000 iterations per second, respectively. As is seen from these histograms, the use of two deformable mirrors (curve 2DMs) resulted in the average metric increase and decrease of the metric fluctuations.

D. Analysis of Compensation Efficiency Based on Imaging Data

Consider now the results obtained with the fast-framing NIR camera located in the image plane of the SPGD_AO system in Fig. 2. The imaging data (movies that contain a set of 500 short-exposure images recorded at a frame rate of 220 frames/s) is an independent information source for adaptive system performance evaluation. The movies were recorded in the different (ON and OFF) operational regimes for the C_AO and SPGD_AO systems described in Section 3.A. Postprocessing of the movies allowed us analysis of the following image-based quality metrics that are independent of the metric J used for adaptive systems operation:

- Sharpness function J_2 , defined as the integral of the squared intensity over imaging chip area [21].
- Image width w , defined as

$$w^2 = \frac{1}{P_0} \int_s |\mathbf{r} - \mathbf{r}_c|^2 I(\mathbf{r}) d^2r, \quad (3)$$

$$\text{where } r_c = \frac{1}{P_0} \int_s \mathbf{r} I(\mathbf{r}) d^2r$$

is the image centroid vector and P_0 is the integral of image plane intensity over sensor area S , referred to here as received light power;

- Power-in-the-bucket metric $J_{\text{PIB}}(d)$ —received power at the camera sensor inside a circular area of diameter d centered with the image centroid;
- Point-source image maximum intensity I_{max} .

Note that in the case when the diameter d equals the diameter of the pinhole in Fig. 2, the metric $J_{\text{PIB}}(d)$ is similar to the metric J actually measured and used for adaptive control. The difference is that the metric $J_{\text{PIB}}(d)$ was linearly proportional to power inside the circular area (bucket), but the metric J used for SPGD control depended on this power logarithmically.

An example of the temporal dynamics of the image quality metrics obtained by processing a short-exposure image stream (movie) for the third magnitude star Delta Ophiuchi (HR 6056) near 45° elevation for different adaptation regimes is presented in

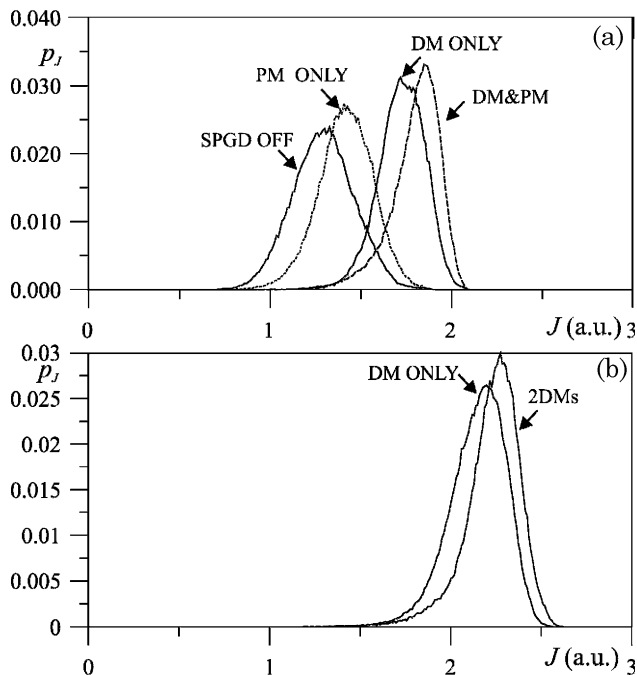


Fig. 7. Probability distributions p_J versus metric J in arbitrary units (a.u.) obtained by averaging 50 adaptation trials with one (a) and with two (b) SPGD controllers. In (a) the SPGD controller PC₁ was used to control the deformable mirror DM₁ (DM ONLY), or PM (PM ONLY), or DM₁ and PM (DM&PM) with the iteration rate 6000 iterations per second. In (b) the SPGD controller PC₂ was used to control the deformable mirror DM₂ with the iteration rate 8000 iterations per second (DM ONLY), and both PC₂ and PC₁ SPGD controllers were used to asynchronously control two deformable mirrors DM₂ and DM₁ with the iteration rates 8000 and 6000 iterations per second, correspondingly (2DMs). The corresponding data were recorded with the C_AO system off, using Antares as a light source at an elevation angle between 16° and 18° (between 9:09 p.m. and 9:30 p.m.) on (a) 18 May and (b) 17 May 2007. The pinhole size for metric measurements was 200 μm .

Fig. 8. Note that the use of either the C_AO or SPGD_AO system alone resulted on average in a relatively small (near 30%) improvement of the image quality as measured by the sharpness function J_2 in Fig. 8(a), while use of both adaptive systems in a cascade (ON/ON regime) led to nearly three times the increase of the sharpness function value, a decrease of the image width from near $425\ \mu\text{m}$ to near $380\ \mu\text{m}$ (Fig. 8(b)), a twofold increase of the power in the bucket metric and in peak intensity value (Fig. 8(c) and 8(d)).

Typical examples of short-exposure images of the star Antares at elevation angles between 11° – 13° are shown in Fig. 9, and between 22° – 25° in Fig. 10. Observation at these elevation angles resulted in highly distorted star images that can be only partially corrected by using either conventional- or SPGD-based AO systems. The characteristic size of the uncompensated star in Figs. 9(a) and 10(a) is significantly larger than the diffraction-limited size (Airy disc diameter) shown by the white circle. Adaptive compensation resulted in a nearly threefold decrease in the image size in the horizontal direction and did not significantly change the image size in the orthogonal direction.

Analysis of the recorded imagery data at low elevation angles shows that images of stars were distorted nonuniformly, exhibiting highly pronounced cigar-type shapes as seen in Figs. 9(a) and 10(a). This type of image distortion is related to an atmospheric refraction effect [22]. Since the nonfluctuating component of the refractive index in the atmosphere is

a function of altitude, the atmospheric layers refract wave components with different wavelengths at slightly different angles. As a result these wave components are angularly separated at the telescope pupil, which in turn leads to an elongation of the corresponding star image. Note that this refraction effect also leads to dependence of phase distortions on the arrival angle (wavelength anisoplanatism), since wave components with different wavelengths do not propagate exactly through the same atmosphere path. Because an adaptive system operates in a relatively narrow wavelength band, compensation efficiency can be highly nonuniform along the axis of the star image elongation (along the long axis of the cigar-shaped star image). This effect is seen clearly in the compensated images in Figs. 9(c) and 10(b)–10(d), where the cigar-shaped star images are noticeably narrower on the left-hand side.

With the use of a narrowband filter this effect can be effectively mitigated. Nevertheless, in our experiments with adaptive compensation we did not use such a filter, since its installation resulted in nearly a 50% decrease in the received optical power and a corresponding undesirable decrease in the signal-to-noise level.

4. Conclusion

The AO experiments over extended atmospheric propagation paths conducted at the 3.63 m telescope in May 2007 resulted in a considerable amount of data. This data shows that the efficiency of adaptive compensation under deep turbulence conditions using

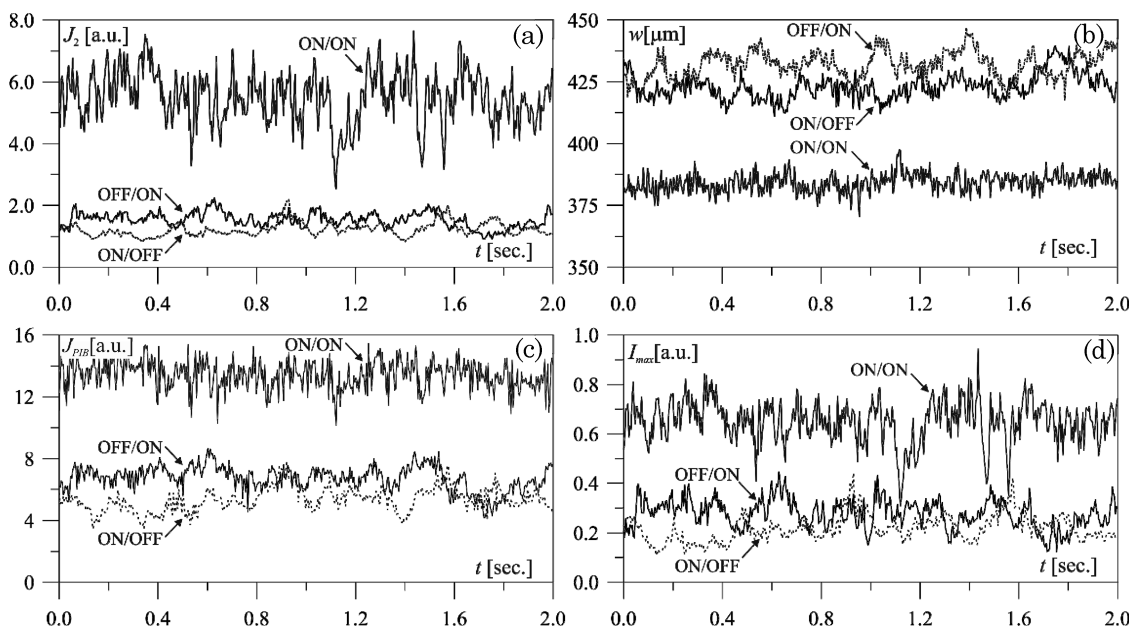


Fig. 8. Temporal dependences of the image quality metrics calculated based on postprocessing of a video-sequence (movie) containing 500 short-exposure NIR images of the third magnitude star Delta Ophiuchi at an $\sim 45^\circ$ elevation angle for the following operational regimes: ON/ON, feedback control is on for both the C_AO system and SPGD AO system with DM_1 and PM deformable mirrors both operating; OFF/ON, feedback control is on for only the SPGD AO system; and OFF/OFF, feedback control is on for only the C_AO system. The image quality metrics are: (a) sharpness function J_2 , (b) star image width w in micrometers; (c) power-in-the-bucket metric J_{PIB} (received light power inside a circular area of $200\ \mu\text{m}$) in arbitrary units (a.u.), and (d) maximum focal plane intensity I_{max} . The SPGD adaptation rate was 4600 iterations per second. The pinhole size was $200\ \mu\text{m}$.

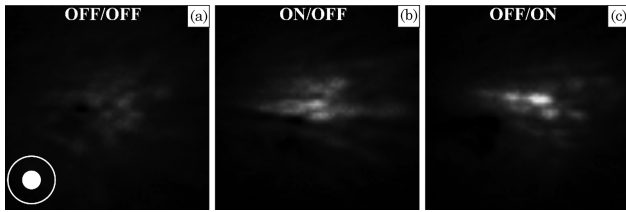


Fig. 9. Short exposure images of the star Antares at low elevation angles (between 11° and 13°) obtained on 18 May 2007 in the cascaded adaptive optical system with the operational regimes (a) OFF/OFF (no AO control), (b) ON/OFF (control is on for only C_AO), and (c) OFF/ON (control is on for only SPGD AO with DM₁). The diffraction-limited image and the pinhole sizes are shown in the bottom left by the white circle and ring, respectively.

either C_AO or SPGD_AO systems, or both (cascaded AO), is highly dependent on a number of factors, such as type, elevation, and magnitude of the stars imaged; atmospheric and weather conditions; control algorithm parameters; metric sensor parameters (pinhole size, photodetector sensitivity); SPGD iteration rate; and efficiency of static and quasi-static aberration precompensation. For this reason rigorous evaluation of the adaptation techniques used cannot be performed without taking into consideration all of these factors. Nevertheless, analysis of the experimental results supports the following observations.

At very low elevation angles ($<10^\circ$) the SPGD adaptive system with one or two deformable mirrors (13 and 26 control channels) performed noticeably better than the C_AO system (941 control channels).

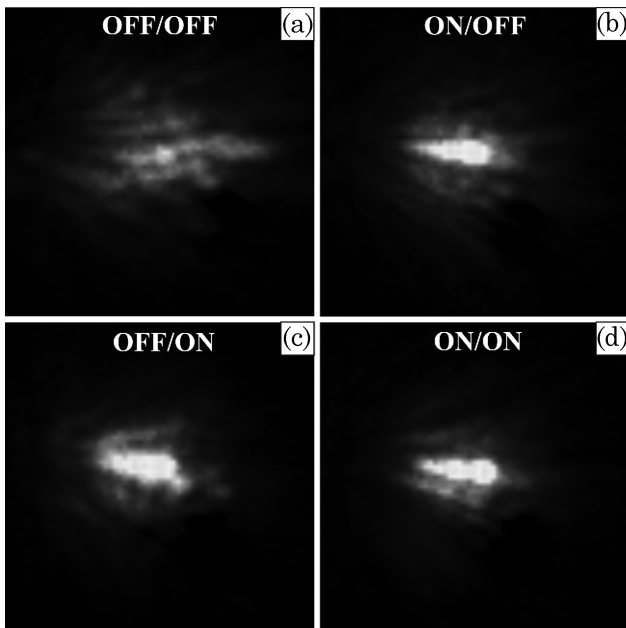


Fig. 10. Short exposure images of the star Antares at low elevation angles (between 22° and 25°) obtained on 18 May 2007 in the cascade adaptive optical system with the operational regimes (a) OFF/OFF (no AO control), (b) ON/OFF (control of only C_AO), (c) OFF/ON (control of only SPGD AO with DM₁), (d) ON/ON (cascaded AO).

Still, the compensation achieved was very poor. Under these atmospheric conditions cascaded compensation with both the C_AO and SPGD_AO systems did not result in performance improvement. Furthermore, activation of the C_AO system while the SPGD_AO system was operating often resulted in adaptation performance degradation.

With observation of a star at higher elevation angles between approximately 15° and 40° aberration compensation performance achieved with either the C_AO or SPGD_AO systems was nearly the same, while the use of both systems in a cascade resulted in a significant improvement of the computed image quality metrics (nearly a threefold improvement for J_2).

With further increases of the elevation angle (above 40° – 45°) compensation with the C_AO system resulted in a better-quality image than was achieved with the SPGD system. Still, the use of the cascaded AO system always resulted in some degree of performance improvement that decreased when the elevation angle was increased.

Preliminary results of an ongoing numerical analysis of cascaded AO systems (not discussed here) show that under severe turbulence conditions typical for wave propagation through distributed turbulence, there are several compelling reasons to reverse the order of adaptive compensation and consider first mitigation of large-scale phase aberrations by using a SPGD feedback control system.

The authors are grateful to W. Bradford for helpful discussions and K. Aschenbach for technical support. This work was supported by the U.S. Joint Technology Office under contract JTO-07-S&A-0238 and by the Cooperative Agreement W911NF-06-2-0009 between the U.S. Army Research Laboratory and the University of Maryland, College Park.

References

1. M. C. Rytov, Yu A. Kravtsov, and V. I. Tatarskii, *Wave Propagation through Random Media*, Vol. 4 of Principles of Statistical Radiophysics (Springer-Verlag, 1989).
2. J. W. Hardy, *Adaptive Optics for Astronomical Telescopes* (Oxford U. Press, 1998).
3. F. Roddier, *Adaptive Optics in Astronomy* (Cambridge U. Press, 1999).
4. T. Weyrauch and M. A. Vorontsov, "Atmospheric compensation with a speckle beacon under strong scintillation conditions: directed energy and laser communication applications," *Appl. Opt.* **44**, 6388–6401 (2005).
5. J. D. Barchers, D. L. Fried, and D. J. Link, "Evaluation of the performance of Hartmann sensors in strong scintillation," *Appl. Opt.* **41**, 1012–1021 (2002).
6. D. L. Fried, "Branch point problem in adaptive optics," *J. Opt. Soc. Am. A* **15**, 2759–2768 (1998).
7. M. Chen, F. S. Roux, and J. C. Olivier, "Detection of phase singularities with a Shack–Hartmann wavefront sensor," *J. Opt. Soc. Am. A* **24**, 1994–2002 (2007).
8. G. A. Tyler, "Reconstruction and assessment of the least squares and slope discrepancy components of the phase," *J. Opt. Soc. Am. A* **17**, 1828–1839 (2000).

9. V. P. Aksenov and O. V. Tikhomirova, "Theory of singular-phase reconstruction for an optical speckle field in the turbulent atmosphere," *J. Opt. Soc. Am. A* **19**, 345–355 (2002).
10. D. L. Fried, "Anisoplanatism in adaptive optics," *J. Opt. Soc. Am.* **72**, 52–61 (1982).
11. R. J. Sasiela, "Strehl ratios with various types of anisoplanatism," *J. Opt. Soc. Am. A* **9**, 1398–1406 (1992).
12. M. A. Vorontsov, G. W. Carhart, and J. C. Ricklin, "Adaptive phase-distortion correction based on parallel gradient-descent optimization," *Opt. Lett.* **22**, 907–909 (1997).
13. M. A. Vorontsov and V. P. Sivokon, "Stochastic parallel gradient descent technique for high-resolution wavefront phase distortion correction," *J. Opt. Soc. Am. A* **15**, 2745–2758 (1998).
14. M. A. Vorontsov, J. F. Riker, G. Carhart, V. S. Gudimetla, L. Beresnev, and T. Weyrauch "Atmospheric turbulence compensation of point source images using asynchronous stochastic parallel gradient descent technique on AMOS 3.6 m telescope," in *Proceedings of AMOS Technologies Conference* (Maui Economic Development Board, 2007). pp. 658–668.
15. M. A. Vorontsov, G. W. Carhart, M. Cohen, and G. Cauwenberghs, "Adaptive optics based on analog parallel stochastic optimization: analysis and experimental demonstration," *J. Opt. Soc. Am. A* **17**, 1440–1453 (2000).
16. T. Weyrauch, M. A. Vorontsov, T. G. Bifano, J. Hammer, M. Cohen, and G. Cauwenberghs, "Micro-scale adaptive optics: wavefront control with μ mirror array and VLSI stochastic gradient descent controller," *Appl. Opt.* **40**, 4243–4253 (2001).
17. L. C. Roberts, Jr., and C. R. Neyman, "Characterization of the AMOS adaptive optics system," *Pub. Astron. Soc. Pacific* **114**, 1260–1266 (2002).
18. L. A. Beresnev, M. A. Vorontsov, and P. Wangsness, "Pocket deformable mirror for adaptive optics applications," in *Proceedings of AMOS Technologies Conference* (Maui Economic Development Board, 2006), pp. 568–575.
19. L. A. Beresnev and M. A. Vorontsov, "Scalable-size deformable pocket mirror with on-pockets bimorph actuators," provisional U.S. patent application 60/984,799 filed 2 November, 2007.
20. M. A. Vorontsov and G. Carhart, "Adaptive wavefront control with asynchronous stochastic parallel gradient descent clusters," *J. Opt. Soc. Am. A* **23**, 2613–2622 (2006).
21. R. A. Muller and A. Buffington, "Real-time correction of atmospherically degraded telescope images through image sharpening," *J. Opt. Soc. Am.* **64**, 1200–1210 (1974).
22. S. V. Kireev and S. V. Sokolovskiy, "Variations of refraction angles from observations of the Moon from space," *Appl. Opt.* **33**, 8402–8405 (1994).